Peer-reviewed version available at *Materials* **2019**, *12*, 4154; doi:10.3390/ma12244154

Article

Scanning Magnetic Microscope Using A Hall-Effect Sensor for Images of Remanent Magnetization Fields

Jefferson F. D. F. Araujo [1,*], Angela A. P. Correa [2], Elder Yokoyama [2], Andre L. A. dos Reis [3], Vanderlei C. Oliveira Jr. [3], Leonardo A. F. Mendoza [4], Marcos A. C. Pacheco [5], Cleanio Luz-Lima [6], Amanda F. Santos [1], Fredy G. Osorio G. [1], Giancarlo E. Brito [7], Wagner W. R. Araujo [7], Tahir Tahir [1], Antonio C. Bruno [1] and Tommaso Del Rosso[1]

[1] Department of Physics, Pontifical Catholic University of Rio de Janeiro, Rio de Janeiro 22451–900, Brazil; afariassantos@aluno.puc-rio.br (A.S.); fosorio@puc-rio.br (F. G.); acbruno@puc-rio.br (A. B.); tommaso@puc-rio.br (T. R.);
[2] Department of Geosciences, University of Brasília, Brasília, Brazil; correaangela@yahoo.com (A. C.); eyokoyama@unb.br (E. Y.)
[3] Department of Geophysics, Observatório Nacional, Rio de Janeiro, Brazil; andrelreis@on.br (A. R.); vanderlei@on.br (V. O.)
[4] Department of Electrical Engineering, Universidade Estadual do Rio de Janeiro, Rio de Janeiro 20550-900, Brazil; mendonza@ele.puc-rio.br (L. M.)
[5] Department of Electrical Engineering, Pontifical Catholic University of Rio de Janeiro, Rio de Janeiro 22451–900, Brazil; marco@ele.puc-rio.br (M. P.)
[6] Department of Physics, Campus Ministro Petrônio Portella, Universidade Federal do Piauí, Teresina 64049-550, PI, Brazil; cleanio@ufpi.edu.br (C. L.)
[7] Institute of Physics, University of São Paulo, Rua do Matão 1371, 05508-090, São Paulo, SP, Brazil; gbrito@if.usp.br (G. B.), wwlysses@usp.br (W. A.)

Abstract - Scanning magnetic microscopy is a new tool that has recently been used to map magnetic fields with good spatial resolution and field sensitivity. This technology has great advantages over other instruments; for example, its operation does not require cryogenic technology, which reduces its operational cost and complexity. Here, we describe the construction of a customizing scanning magnetic microscope based on commercial Hall-effect sensors at room temperature that achieves a spatial resolution of 200 μm. Two scanning stages on the x- and y-axes of precision, consisting of two coupled actuators, control the position of the sample, and this microscope can operate inside or outside a magnetic shield. We obtained magnetic field sensitivities better than 521 $nT_{rms}/\sqrt{Hz}$ between 1 and 10 Hz, which correspond to a magnetic momentum sensitivity of 9.20×10^{-10} Am^2. In order to demonstrate the capability of the microscopy, polished thin sections of geological samples, samples containing microparticles and magnetic nanoparticles were measured. For the geological samples, a theoretical model was adapted from the magnetic maps obtained by the equipment. Vector field maps are valuable tools for the magnetic interpretation of samples with a high spatial variability of magnetization. These maps can provide comprehensive information regarding the spatial distribution of magnetic carriers. In addition, this model may be useful for characterizing isolated areas over samples or investigating the spatial magnetization distribution of bulk samples at the micro and millimeter scales. As an auxiliary technique, a magnetic sweep map was created using Raman spectroscopy; this map allowed the verification of different minerals in the samples. This equipment can be useful for many applications that require samples that need to be mapped without a magnetic field at room temperature, including rock magnetism, the nondestructive testing of steel materials and the testing of biological samples. The equipment can not only be used in cutting-edge research but also serve as a teaching tool to introduce undergraduate, master's and Ph.D. students to the measurement methods and processing techniques used in scanning magnetic microscopy.

Keywords: scanning magnetic microscopy; Hall sensor; magnetic measurements; geological sample

1. Introduction

Rock magnetism studies seek to retrieve information regarding primordial magnetic fields in terrestrial and extraterrestrial rocks by analyzing their remanent magnetizations. However, the direct measurement of magnetization within a rock sample cannot be performed using currently available techniques. Therefore, it is necessary to estimate the magnetization from measurements of the magnetic field outside of the sample produced by its remanence. Scanning magnetic microscopes are a relatively recent class of instruments capable of mapping this external field at fine spatial scales, which is essential for obtaining magnetization images. Most scanning magnetic microscopes require a cryogenic system, so their operation and maintenance are generally expensive, rendering them unfeasible for most low-cost laboratories [1-3]. Scanning magnetic microscopes using nonsuperconducting devices have recently been proposed in the literature, some of them for geological applications [4-6].

In this article, we propose the development of a scanning magnetic microscope for the magnetic characterization of millimeter-scale samples in an environment protected or not protected by a magnetic shield. Using both samples of magnetic microparticles with a low mass (60 μg) and geological samples, the configuration used can measure the remanent magnetic fields of the samples in the z direction, i.e., perpendicular to the sample. The device has a scanning range from 150 mm to 150 mm with micrometer resolution. In the current configuration, the microscope is equipped with commercial Hall-effect sensors. The output noise measured at 6.0 Hz is approximately 521 nT_{rms} / √Hz in a protected environment, and the magnetic moment sensitivity is 9.20×10^{-10} Am^2 [6-9]. A low-cost device capable of filtering and amplifying the signals collected by the Hall-effect sensors, with the same quality as similar equipment offered in the market, was also developed, making it accessible and operational in academic environments. We tested the device's performance with magnetic microparticles containing a core of iron oxide and geological samples.

In addition, a theoretical model was adapted to analyze the data. This model is different from most of the models currently used to analyze scanning magnetic microscopy data. The majority of the theoretical models are developed based on only one magnetic dipole representing the geological sample as if it were totally uniform. Through this model, it is possible to obtain the magnetic moment of the whole sample. However, the results obtained from the magnetic maps and from Raman spectroscopy showed that the analyzed geological samples are not uniform, and this fact cannot be neglected. The model used in this study is based on the equivalent-layer method to invert the vertical component of the magnetic field generated by the geological sample. The equipment developed here can be easily reproduced and used in low-cost laboratories as well as in classrooms used to teach physics, engineering, geophysics, and geology. A program was also developed to automate both the data acquisition and the positioning motor movement. Thus, acquisition is fast and versatile, and data can be obtained from a wide range of magnetic samples of different sizes, resulting in many advantages, such as short acquisition time and the possibility of focusing on certain positions in the XY space.

2. Magnetic microscope

2.1. Mechanical design and Hall sensors

The magnetic microscope is capable of scanning magnetic samples (bulk, liquid, micro- or nanostructured), which are placed in the sample port (Figure 1a and 1b). The sample is placed face up (positive direction, z-axis) on the sample holder using adhesive tape (Figure 1 (b)). In order to detect the response generated by the sample, we used two commercial Hall sensors (AWM, Co.),

Peer-reviewed version available at Materials 2019, 12, 4154; doi:10.3390/ma12244154

hereinafter referred to as Sensor A and Sensor B, which incorporate an GaAs element in a surface-mount technology (SMT) package. The sensor detection areas are 200 μm in diameter, and they have a distance of 125 μm (after calibration) to the upper surface. Both sensors are connected in an axial gradiometric configuration and are fixed on the opposite sides of a printed circuit board (Figure 1c).

Sensor A is fixed to the circuit board next to the sample with a clear epoxy resin. To approach the sample, sensor A is cut until its 4 connecting terminals appear on the upper surface. Sensor B acts to reduce the external noise that the shield is unable to eliminate. The circuit board is mounted on a fixed acrylic frame.

We can influence the sensors by adjusting the current or voltage. After several tests, we concluded that polarization by current in the 0.5 mA – 4.5 mA range produced the best signal-to-noise ratio [10]. The circuit consisted (see Figure 2a) of current sources and instrumentation amplifiers for the amplification. A low-noise preamplifier was built (the lock-in that we constructed, hereafter referred to using the following abbreviation: AJE amplifier) and acts as a gradiometer by electronically subtracting the two output signals.

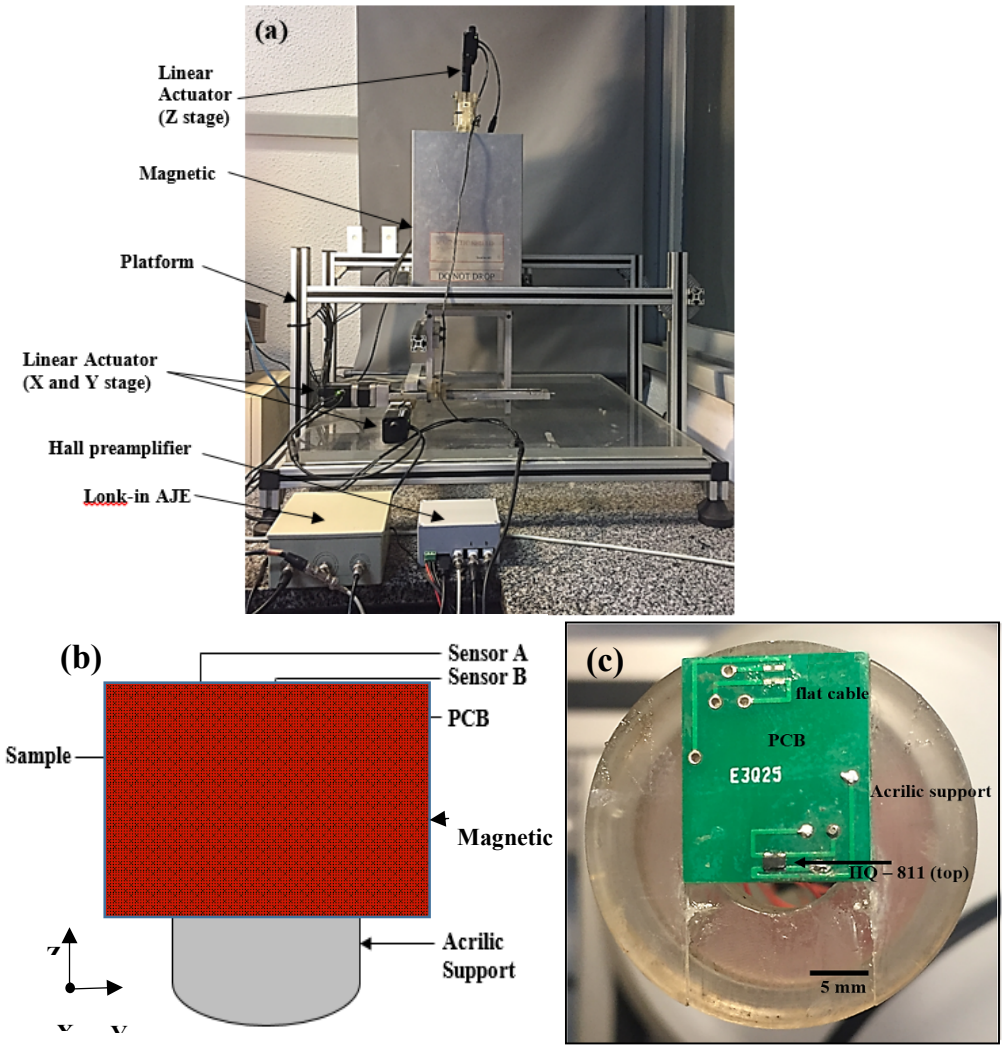

Figure 1. (**a**) Image of the Hall microscope and its components. (**b**) Diagram of the main components of the microscope: circuit board containing the gradiometric sensors (A and B), sample holder, which moves in the X and Y directions. All equipment is inside a magnetic shield. The diagram is not drawn to scale. (**c**) Photo of the Hall sensors coupled in an acrylic structure.

Peer-reviewed version available at Materials 2019, 12, 4154; doi:10.3390/ma12244154

In the assembly, the current sources were based on the IC LM334, which is resistance-controlled and shows high noise and a strong temperature dependence [10]. Next, we redesigned the circuit, replacing the LM334 with the AMP03 with the two current sources, which are controlled by voltage, and we achieved better results. Figure 2b shows a comparison between the noise spectra of the two custom electronic devices, one with the AMP03 electronics and the fabricated lock-in AJE amplifier and the other with the commercial lock-in amplifier (SR560, SRS Inc.). We used an alternating current at a frequency of 1.0 kHz and a peak amplitude of 1.0 V [1,11]. For comparison purposes, we added a magnetic signal at 4 Hz to the measurements.

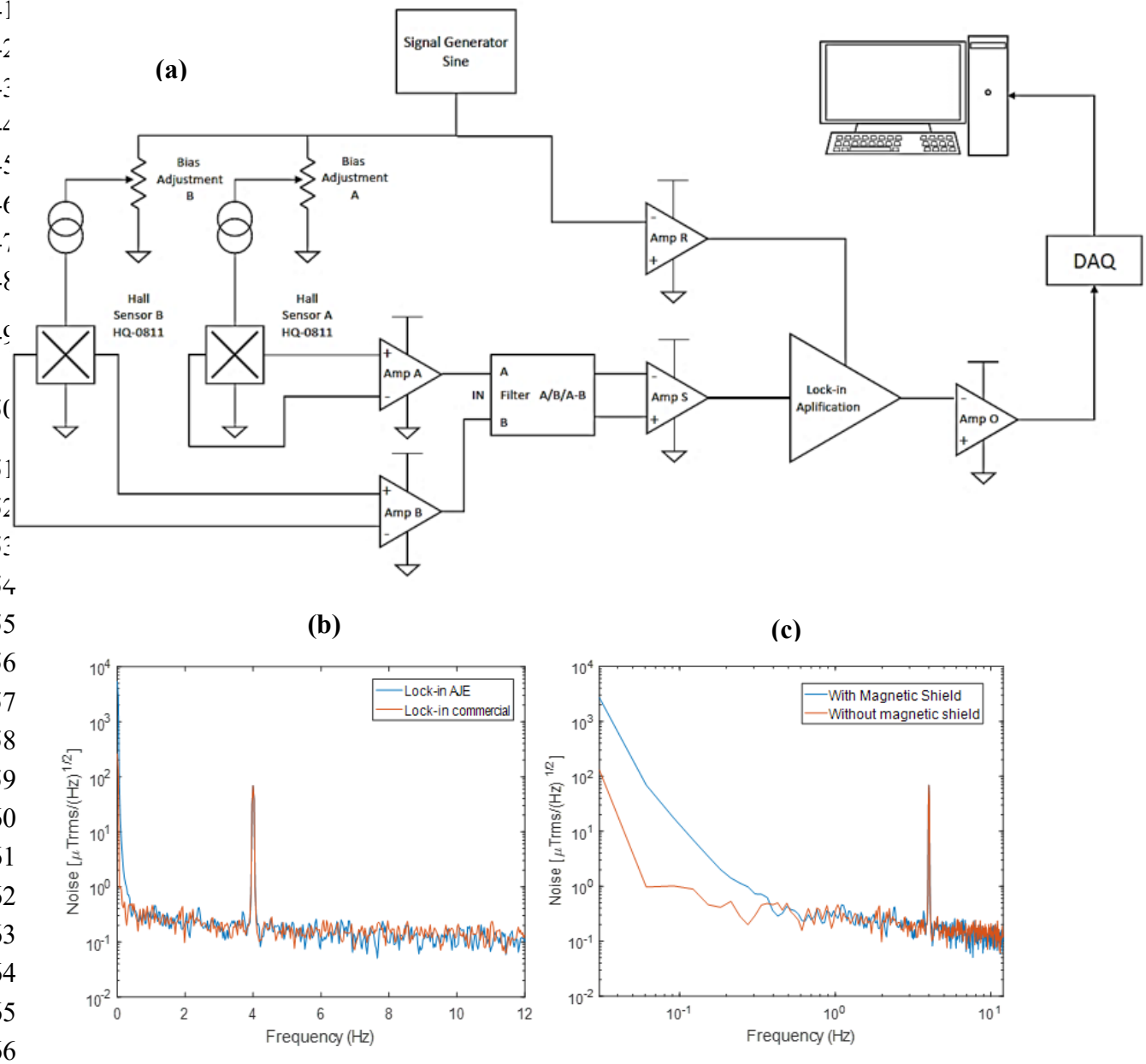

Figure 2. (a) Circuit consisting of current sources and instrumentation amplifiers for the amplification . (b) Noise analysis graph between the lock-in AJE equipment and the commercial lock-in equipment. (**c**) Noise analysis graph of the gradiometer system with and without the protection of the magnetic shield.

We can observe in Figure 2b that, under these conditions, there is virtually no difference between the two configurations (the lock-in AJE amplifier and the commercial lock-in equipment),

Preprints (www.preprints.org) | NOT PEER-REVIEWED | Posted: 18 October 2019 doi:10.20944/preprints201910.0210.v1

Peer-reviewed version available at Materials 2019, 12, 4154; doi:10.3390/ma12244154

and the preamplifier (the lock-in AJE amplifier) has low operating costs. We also conducted noise tests with and without the magnetic shield (See Figure 2c) and once again observed that there is no difference in the readings of the gradiometer system with and without the protection of the magnetic shield, which is necessary for some geological samples.

2.2. Lock-in AJE amplifier

In the assembly of the lock-in AJE amplifier (Figure 3), components found in the domestic market were used in the laboratory and were applied according to the technical specifications of the integrated circuits (ICs) used. The following components were selected for the assembly of the electrical circuit: an AD620 amplifier, an AD630 synchronous demodulator, an OP27 amplifier, a function generator in the 8 - 90 kHz range, a digital oscilloscope, wires, solder, a protoboard, male/female connectors, 10 µF electrolytic capacitors, a 0.47 µF disk capacitor, a 100 µF electrolytic capacitor, a 100 µF-1000 pF condenser, 10 Ω resistors, a 1 MΩ resistor, a 10 KΩ resistor, a 1 KΩ resistor, a 100 KΩ resistor, a 10 K potentiometer or resistance box for amplifier gain, and a power supply of +/- 15 V.

Using the help of the Proteus 8.1 software, which is specialized for electronic circuit designs, the components were assembled according to the electronic circuit diagram shown in the figure below.

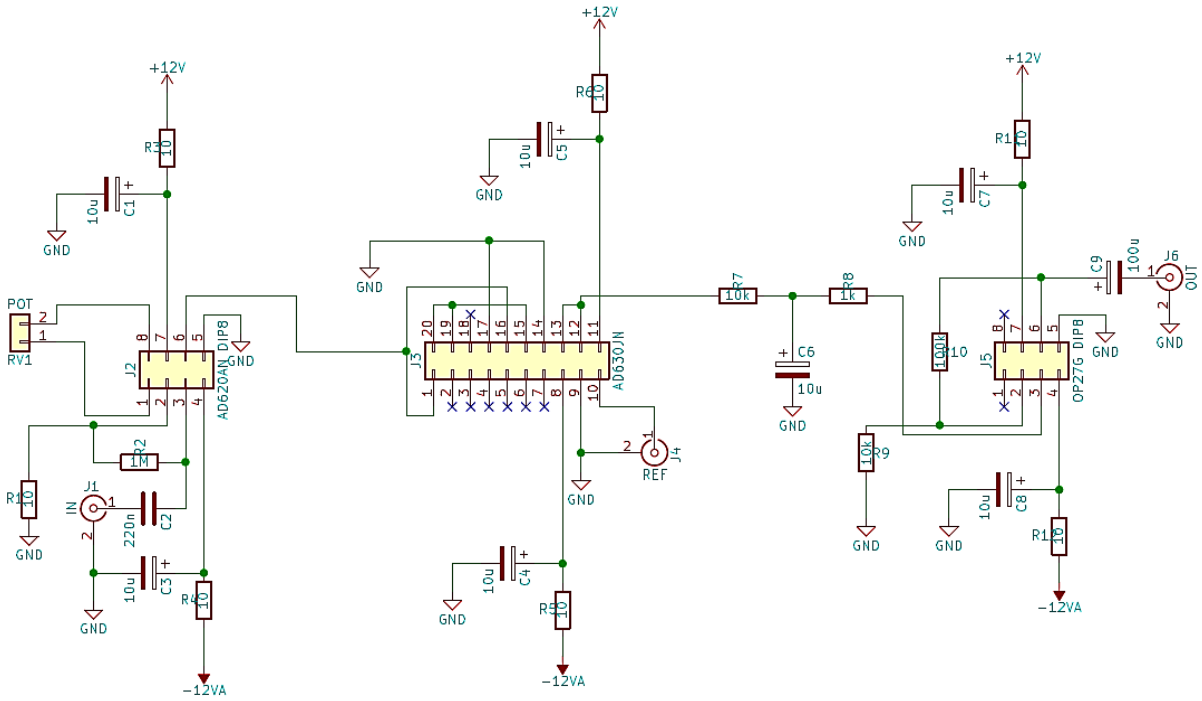

Figure 3. Electric circuit of a lock-in amplifier using the AD620, AD630, and OP27 integrated circuits.

Among the electronic components offered in the market, the operation of three ICs stood out when the objective was to assemble a specific amplification circuit with phase adjustment. The ICs selected for the manufactured lock-in amplifier are listed below.

The AD620, used as the initial amplifier, amplifies the signal applying a variable gain resistance. Since the amplifier amplifies not only the desired signal but also the signal as a whole, the noise is also amplified. Therefore, an appropriate sensitivity setting should be chosen.

The AD630 synchronous demodulator, which is an essential component in the lock-in amplifier, mixes the real signal to form the input reference signal.

The OP27G, a low-pass amplifier, filters out any noise in the modulated signal and produces the desired DC signal, which determines the filtering level. Given the technical characteristics of these ICs, one can assemble an electrical circuit.

In preliminary tests, the AD620 amplifier received the signal from the function generator, simulating the signal obtained by the magnetic probe, and amplified its voltage according to the adjustments made in the potentiometer. The operation was based simply on a noninverting operating amplifier. The circuit was powered by the +/- 15 V power source, with low-pass filters connected to each source to filter out any undesirable circulating noise. The disk capacitor worked by avoiding fluctuations in the signal when performing demodulation on the road. A reference signal, also provided by the signal generator, was introduced into the demodulator for signal mixing because this component is the signal input port to the demodulator. The synchronous demodulator (AD630) received the output signal from the input amplifier and multiplied it with the reference input. The final component of the lock-in amplifier, the OP27 low-pass amplifier, was intended to filter all unwanted signals and produce a DC (direct current) signal that indicates the field strength.

3. Results

3.1. Calibration and magnetic measurements

The calibration process of the magnetic microscope consists of acquiring the distance on the z-axis between the sensitivity region of the Hall-effect sensors and the surface of the sample using only circuit boards and measuring the sample remanent fields, with a 99% purity nickel sphere magnetized at 0.5 T to determine the distance. The nickel sphere was placed in a sample holder made of acrylic material with a cylindrical cavity (see Figure 4a). Figure 4b shows the map of the remanent magnetic field of the nickel sphere. Using the magnetic map and the model of a magnetic dipole, the magnetic moment of the nickel sphere was determined [5-10]. After finding the magnetic moment of the nickel sphere, it is possible to estimate the distance between the sensitivity region of sensor A and the surface of the sample, which was approximately 115 μm. This number has been confirmed using synthesized by pulsed laser ablation (PLA) in liquid. We use sample with low mass, in the range of with mass on the order of tens of μg. This calibration is very important because it is through this calibration that we have the accuracy of the equipment.

Preprints (www.preprints.org) | NOT PEER-REVIEWED | Posted: 18 October 2019 doi:10.20944/preprints201910.0210.v1

Peer-reviewed version available at Materials 2019, 12, 4154; doi:10.3390/ma12244154

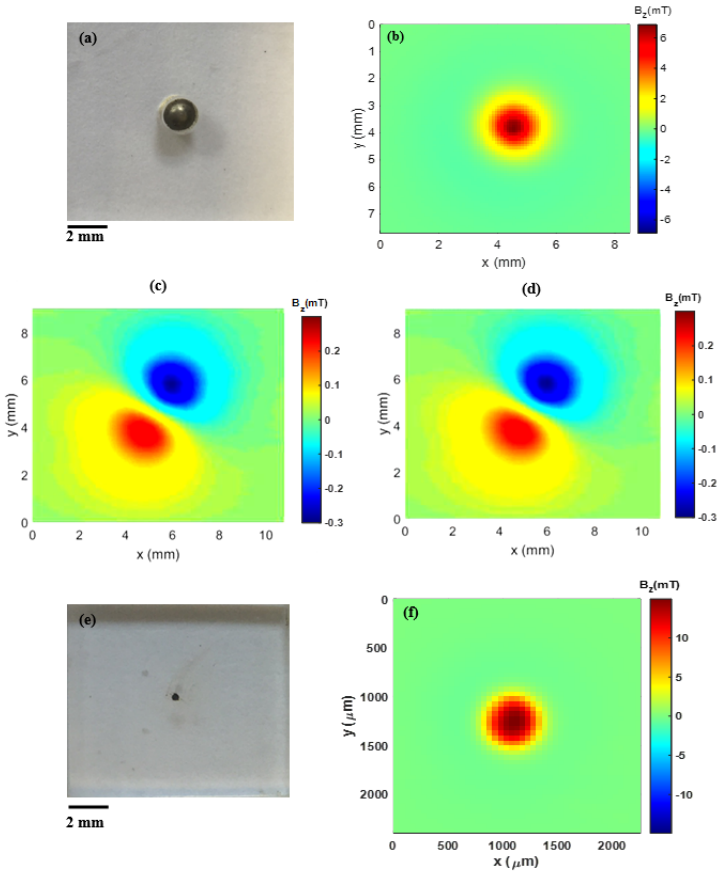

Figure 4. (**a**) Acrylic sample holder with a cylindrical cavity in which the 99% purity nickel sphere was placed. (**b**) Magnetic map of the remanent field of the nickel sphere after being magnetized by a 0.5 T magnetic field. (**c**) Magnetic map of the remanent field of the same sphere measured using only circuit boards after a demagnetization process. (**d**) Magnetic map of the remanent field of the same sphere measured using the commercial lock-in amplifier after a demagnetization process. (**e**) Figure representing microparticles of iron oxide. (**f**) Magnetic map of the remanent field of iron oxide microparticles.

In order to verify the assembly capability, we used only circuit boards and compared the measurements with magnetic maps obtained with commercial equipment, such as the lock-in amplifier (SR560, SRS Inc.) using the same 99% purity nickel sphere, which was analyzed after being magnetized by a 0.5 T field, and magnetic microparticles of Fe_3O_4 obtained by the coprecipitation method [10-12]. Thus, we made scanning magnetic maps of the x- and y-axes (Figure 4c – 4f). Unlike the calibration process, the maps of Figure 4c and 4d were obtained after the nickel sphere was demagnetized. After this process, the scanning magnetic map was prepared. Figure 4c shows the map obtained using only circuit boards, while the map in Figure 4d shows the map obtained using the commercial lock-In equipment (SR560, SRS Inc.). The intensity of the remanent magnetic field in these maps (Figure 4c – 4d) is lower than that in Figure 4b by an order of magnitude due to the demagnetization process. Notably, there is essentially no difference in the magnetic maps of the partially demagnetized spheres. This result is in agreement with the graph in Figure 2b.

We also mapped the remanent field of Fe_3O_4 microparticles obtained by the coprecipitation method. Approximately 50 μg of magnetic Fe_3O_4 microparticles were placed in a cylindrical cavity in the acrylic sample holder, which has a diameter of 400 μm and a depth of 400 μm (Figure 4e). Figure 4f shows the map of this cylindrical cavity. Through the magnetic map, we can obtain the moment using a model of a cylinder that takes the shape of the sample in the cylindrical cavity. In addition, we can also map the remanent fields of magnetic nanoparticles produced by laser ablation that have very small diameters. This type of magnetic map and magnetic moment obtained by magnetic

Peer-reviewed version available at Materials 2019, 12, 4154; doi:10.3390/ma12244154

microparticle scanning microscopy may be important for a number of applications such as *in vitro* and *in vivo* studies.

3.2. Geological samples

To test the efficiency of the present microscopy on the natural samples, we have choosed two different geological samples to essey. A short overview of the geological context of these samples will be explaned as follows.

3.2.1. Parnaíba sample

Continental magmatic events have been recorded on several tectonic provinces at the South America Platform [13]. These events included the formation of dikes, sills and flows of basaltic rocks that occur in both sedimentary basins and orogenic belts. The Parnaíba Basin is one of the largest cratonic sedimentary basins in South America, with an area of 665,888 km^2. The basin is bordered to the west by the Tocantins Province and to the east by the Borborema Province. The basaltic rocks (Figure 5a) of Parnaíba are related to the opening of the Atlantic Ocean, both at the Triassic-Jurassic bondary and at the Early Cretaceous period.

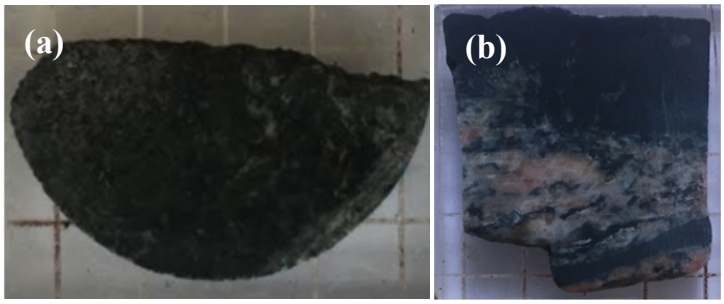

Figure 5. (**a**) Photo representing a sample taken from the Brazilian state of Tocantins. (**b**) Photo representing the Vredefort sample.

In this study, we collected samples from the basaltic dikes of Paraíso do Tocantins City, located at the western border of the Parnaíba Basin, in its local basement. The dikes host rocks were formed by metamorphic rocks from the Araguaia Fold Belt. By geological field control, we have estimed that these dikes belong to the Triassic-Jurassic Bondary volcanic suite.

3.2.2. Vredefort sample

Impact cratering is the fastest known geological process. High shock pressures (> 5 GPa) and high shock temperatures (> 1000°C) are responsible for the formation of unique geochemical systems. The evolution of these systems, i.e., the formation of new mineralogy, can generate complex petrophysical signatures [14-16]. An example of this kind of signature can be observed on the rock magnetic data of the Vredefort Dome (South Africa) [17]. The Vredefort Dome is the largest impact structure known on Earth, with a diameter of approximately 250 km, and magnetic studies of the dome have been performed since the 1960s [18-19]. Vredefort has several types of impactites, i.e., impact melt veins, granophyric dikes, shatter cones, etc. In this context, a recurrent target of paleomagnetic studies is the impact melt veins, especially the pseudotachylite veins. Pseudotachylites or pseudotachylite breccia are very fine grained or glassy rock formed mainly by friction melt. This kind of rock has been reported in many failure and shear zones and in some impact structures, such as the Vredefort Dome [20-21].

Preprints (www.preprints.org) | NOT PEER-REVIEWED | Posted: 18 October 2019 doi:10.20944/preprints201910.0210.v1

Peer-reviewed version available at Materials 2019, 12, 4154; doi:10.3390/ma12244154

In this study, we have used samples of the pseudotachylite veins collected on the Leeukop Quarry at the Vredefort Dome during a 2008 field trip (Figure 5b). These samples are similar to those used by for paleomagnetic studies.

3.3. Estimating the magnetic field vector of a rock sample

Measurements of a single component of the magnetic field contain information regarding the other components. For this reason, maps of the *x*- and *y*-components of the magnetic field can be estimated from the *z*-component measurements. Vector field maps are valuable tools for the magnetic interpretation of samples with a high spatial variability of magnetization. These maps can provide comprehensive information regarding the spatial distribution of magnetic carriers. Moreover, field maps can be useful for characterizing isolated areas over the samples or investigating the spatial magnetization distribution of bulk samples at submillimeter and millimeter scales. The amplitude of the magnetic field vector calculated from three estimated components can also show regions devoid of magnetic sources. There are several techniques for estimating the three components of the magnetic field in the Fourier domain [22-23] or in the spatial domain by using an equivalent-layer technique [24-25]. However, the equivalent-layer approach does not require evenly spaced data or measurements over a plane above the sample.

We illustrate in this section how the equivalent-layer technique can be used to estimate the three components of the magnetic field using magnetic microscopy data. We applied this method in a metamorphic rock from the Vredefort Dome in South Africa. Given the magnetization direction of the geological sample, we estimate a magnetic moment distribution over the equivalent layer by solving an inverse problem and then calculate the three components of the magnetic field.

3.3.1. Forward and inverse problem

Consider a right-handed Cartesian coordinate system with *z* being oriented positively downward, *x* to the north, and *y* to the east. Let $\boldsymbol{B_z^0}$ be the $N \times 1$ vector whose the ith element $\boldsymbol{B_z^i}$ is the *z*-component of the induction magnetic field at the observation point (x^i, y^i, z^i) over a plane above a rock sample. In order to estimate the other magnetic field components, we use a layer composed of *M* dipoles with unit volume, all of them positioned at a constant depth of $z = h$. Mathematically, the predicted *z*-component of magnetic field produced by the set of dipoles at the point (x^i, y^i, z^i) is given by

$$B_z^i = \sum_{j=i}^{M} m^i a_z^{ij} \quad (1)$$

where m^i is the magnetic moment of the *j*th dipole and

$$a_z^{ij} = \gamma_m M_z^{ij} \hat{\boldsymbol{m}} \quad (2)$$

in which γ_m is a constant proportional to the vacuum permeability, M_z^{ij} is a 3×1 vector equal to

$$M_z^{ij} = [\partial_{xz}\phi^{ij} \; \partial_{yz}\phi^{ij} \; \partial_{zz}\phi^{ij}]^T \quad (3)$$

where $\partial_{\lambda z}\phi^{ij}$, $\lambda = x, y, z$, is the second derivative with respect to the Cartesian coordinates x^i, y^i and z^i of the scalar function

$$\phi^{ij} = \frac{1}{\sqrt{(x^i - x^j)^2 + (y^i - y^j)^2 + (z^i - h\ )^2}} \quad (4)$$

in which x^i, , y^i and h are the Cartesian coordinates of the jth dipole composing the layer. The $\hat{\boldsymbol{m}}$ is a 3 × 1 unit vector with the magnetization direction of all equivalent sources equal to

$$\hat{\boldsymbol{m}} = \begin{bmatrix} \cos I \ \cos D \\ \cos I \ \sin D \\ \sin I \end{bmatrix}, \quad (5)$$

where the I and D are the inclination and declination, respectively. This modeling is solved by using a Python library called Fatiando a Terra [26]. In matrix notation, the predicted z-component of magnetic field produced by the model is given by

$$\boldsymbol{B}_z^p = \boldsymbol{A}_z \boldsymbol{m} \quad (6)$$

in which $\boldsymbol{B}_z^p$ is an N-dimensional vector whose ith element is the predicted z-component of the magnetic field at the point (x^i; y^i; z^i), $\boldsymbol{A}_z$ is an $N \times M$ sensitivity matrix whose ijth element is defined by the harmonic function a_z^{ij} (Equation 2), and $\boldsymbol{m}$ is the M-dimensional parameter vector whose jth element is the magnetic moment of the jth positioned at the point (x^i, y^i, h). Moreover, the parameter vector $\boldsymbol{m}$ represents the magnetic moment distribution over the layer.

The inverse problem consists in estimating the magnetic moment distribution that minimizes the difference between the observed data $\boldsymbol{B}_z^0$ and the predicted data $\boldsymbol{B}_z^p$ (Equation 6). In order to estimate a stable solution $\boldsymbol{m}^*$, we solve the constrained problem of minimizing the goal function

$$\Upsilon(\boldsymbol{m}) = \left\| \boldsymbol{B}_z^0 - \boldsymbol{B}_z^p(\boldsymbol{m}) \right\|_2^2 + \mu \|\boldsymbol{m}\|_2^2 \quad (7)$$

where the first and the second terms of Equation 7 are the data-misfit function and the zeroth-order Tikhonov regularization function, respectively, μ is the regularizing parameter and $\| \, . \, \|_2^2$ denotes the squared Euclidian norm. The least-squares estimate of the parameter vector $\boldsymbol{m}^*$ is given by

$$\boldsymbol{m}^* = (\boldsymbol{A}_z^T \boldsymbol{A}_z + \mu \boldsymbol{I})^{-1} \boldsymbol{A}_z^T \boldsymbol{B}_z^0 \quad (8)$$

Preprints (www.preprints.org) | NOT PEER-REVIEWED | Posted: 18 October 2019 doi:10.20944/preprints201910.0210.v1

Peer-reviewed version available at Materials 2019, 12, 4154; doi:10.3390/ma12244154

in which the superscript T stands for a transposition and $\mathbf{I}$ is the identity matrix of order M. After estimating the magnetic moment distribution $\boldsymbol{m}^*$, we can calculate the two other components of the magnetic field using the relations

$$\boldsymbol{B}_x^p = \boldsymbol{A}_x \boldsymbol{m}^* \tag{9}$$

and

$$\boldsymbol{B}_y^p = \boldsymbol{A}_y \boldsymbol{m}^* \tag{10}$$

in which $\boldsymbol{B}_x^p$ and $\boldsymbol{B}_y^p$ are, the N-dimensional predicted vectors of the x- and y-components of the magnetic field, respectively, and $\boldsymbol{A}_x^p$ and $\boldsymbol{A}_y^p$ are $N \times M$ matrices whose ijth elements are respectively given by

$$a_x^{ij} = \gamma_m M_x^{ij} \hat{\boldsymbol{m}}, \tag{11}$$

and

$$a_y^{ij} = \gamma_m M_y^{ij} \hat{\boldsymbol{m}}, \tag{12}$$

where

$$M_x^{ij} = [\partial_{xx}\phi^{ij}\, \partial_{xy}\phi^{ij}\, \partial_{xz}\phi^{ij}]^T \tag{13}$$

and

$$M_y^{ij} = [\partial_{yx}\phi^{ij}\, \partial_{yy}\phi^{ij}\, \partial_{yz}\phi^{ij}]^T \tag{14}$$

in which $\partial_{\lambda z}\phi^{ij}$, $\lambda = x, y$ the second derivatives of the scalar function ϕ^{ij} with respect to the Cartesian coordinates x^i, y^i and z^i of the observation points, analogous to Equation 2. Finally, We can calculate the amplitude of the magnetic field as follows:

$$\boldsymbol{B} = \sqrt{\boldsymbol{B}_x^{p^2} + \boldsymbol{B}_y^{p^2} + \boldsymbol{B}_z^{p^2}} \tag{15}$$

Preprints (www.preprints.org) | NOT PEER-REVIEWED | Posted: 18 October 2019 doi:10.20944/preprints201910.0210.v1

Peer-reviewed version available at Materials 2019, 12, 4154; doi:10.3390/ma12244154

where $\boldsymbol{B}_x^p$, $\boldsymbol{B}_y^p$ and $\boldsymbol{B}_z^p$ are the *x*-, *y*- and *z*-components of the magnetic field, respectively, and $\boldsymbol{B}$ represents the amplitude.

3.3.2. Magnetic microscopy data application for the Vredefort sample

The observed data were measured on a regular grid of 121 x 99 (a total number of N = 11979 observations) over an area extending 36 mm and 30 mm along the *x*-axis and *y*-axis, respectively (Figure 6a). The sensor-to-sample distance was 138 μm. We use a layer formed by a grid of 121 x 99 dipoles (a total of M = 11979 equivalent sources) positioned at a constant depth of z = 750 μm. The magnetization direction for all dipoles is equal to 90° and 0° for inclination and declination, respectively, that the same direction as the imparted field.

By solving Equation 8 using a regularizing parameter $\mu = 10^{-19}$, we estimate a magnetic moment distribution over the layer (not shown). Figure 6b is the predicted data produced by the equivalent layer. Figure 6c shows the residuals map, that is, the difference between the observed data (Figure 6a) and the predicted data (Figure 6b). The histogram of residuals appears with a mean of 0 mT and a standard deviation of 0.002 mT. It means that the estimate magnetic moment distribution produces an acceptable data fitting. Figure 7a, 7b and 7c shows the predicted *z*-, *x*- and *y*-components of the magnetic field, respectively. We calculate the amplitude of the magnetic field using the estimated three components (Figure 7d). The result shows a concentration of magnetic carriers on the upper bound of the Vredefort sample. In this section, we show an application of the equivalent-layer technique to invert the vertical component of the magnetic field generated by the Vredefort sample. Different from the Fourier domain approach, we calculate the three component and the amplitude of the magnetic field formulating an inverse problem in spatial domain. As shown in the present results (Figure 6 and 7), we conclude that the equivalent-layer technique can be a useful tool for determining the magnetic vector and describing the magnetic carriers within a geological sample.

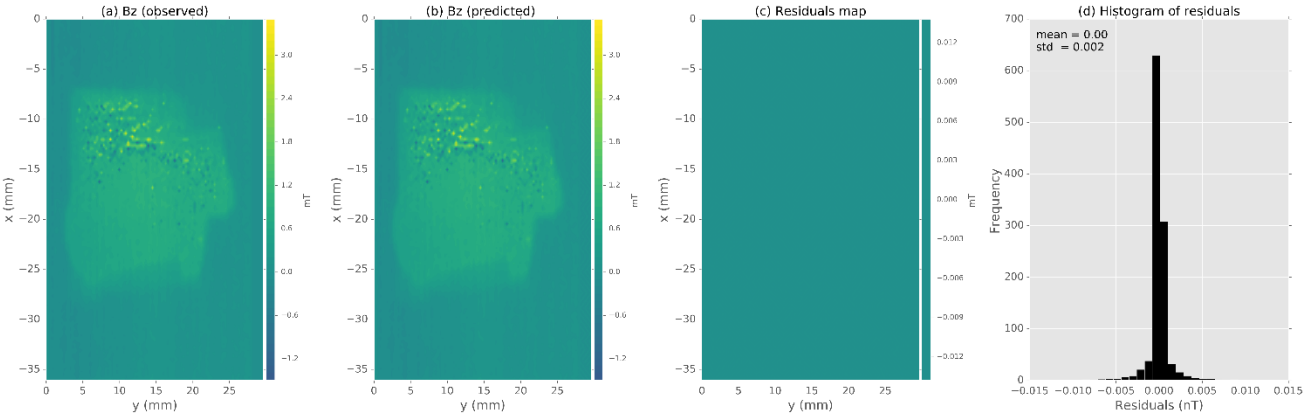

Figure 6. Application to microscopy data from the Vredefort sample. (**a**) Observed z-component measured by the magnetic microscope. (**b**) Estimated z-component produced by the layer. (**c**) Difference between panels a and b. (**d**) Histogram of the residuals.

Peer-reviewed version available at *Materials* **2019**, *12*, 4154; doi:10.3390/ma12244154

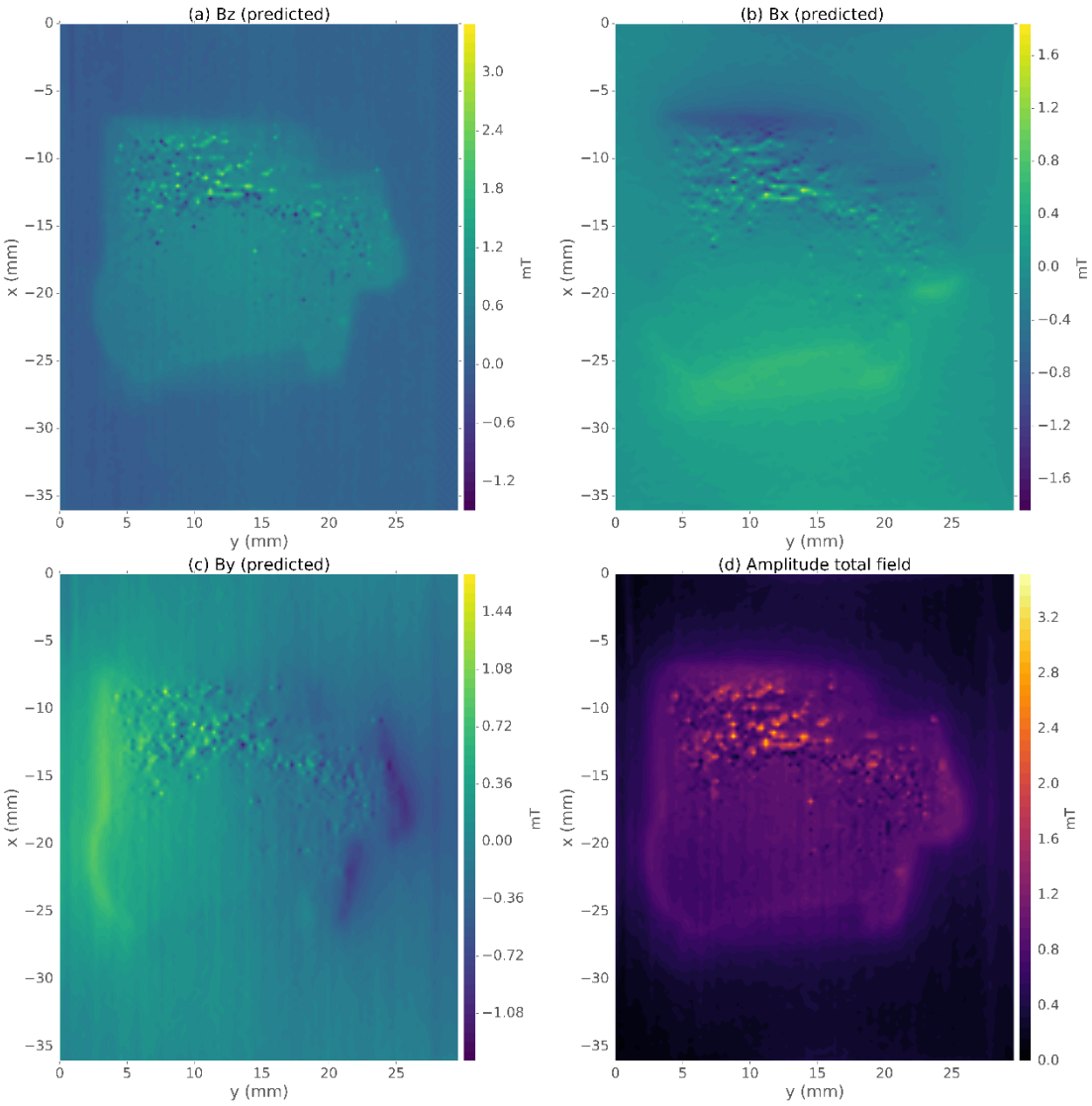

Figure 7. Application to microscopy data from the Vredefort sample. (**a**) Map of the z-component produced by the layer. (**b**) Map of estimated x-component. (**c**) Map of the estimated y-component. (**d**) Amplitude calculated from the estimated magnetic field components.

3.4. Raman spectroscopy

After analyzing the magnetic field images of the geological samples and applying the theoretical model to the Parnaíba and Vredefort samples, we observed a range of magnetic field intensities from -0.1 to 0.1 mT and 0.02 to 0.02 mT for the Parnaíba (Figure 8a) and Vredefort (Figure 9a) samples, respectively. Thus, Raman spectroscopy analysis was performed to verify the presence of different minerals in these samples, mainly the minerals of the regions indicated in the magnetic field figures. Therefore, we confirmed the variation in the intensities and the configuration of the magnetic field measured in the magnetic microscope.

The Raman analyses were performed using a micro-Raman Senterra Bruker spectrometer. The source of excitation was a laser with $\lambda = 785$ nm. The spectrometer slit was adjusted to a resolution of 4 cm^{-1}. An Olympus optical microscope (Olympus BX-50) with an Olympus MPlan 10×0.25 nA lens was applying to focus the sample surface and obtain the images (Figure 8b and Figure 9b) and the Raman spectra (Figure 8c-f). The spectra were obtained in the spectral region from 100 to 3500 cm^{-1}, with 5 accumulations of 20 s.

Peer-reviewed version available at Materials 2019, 12, 4154; doi:10.3390/ma12244154

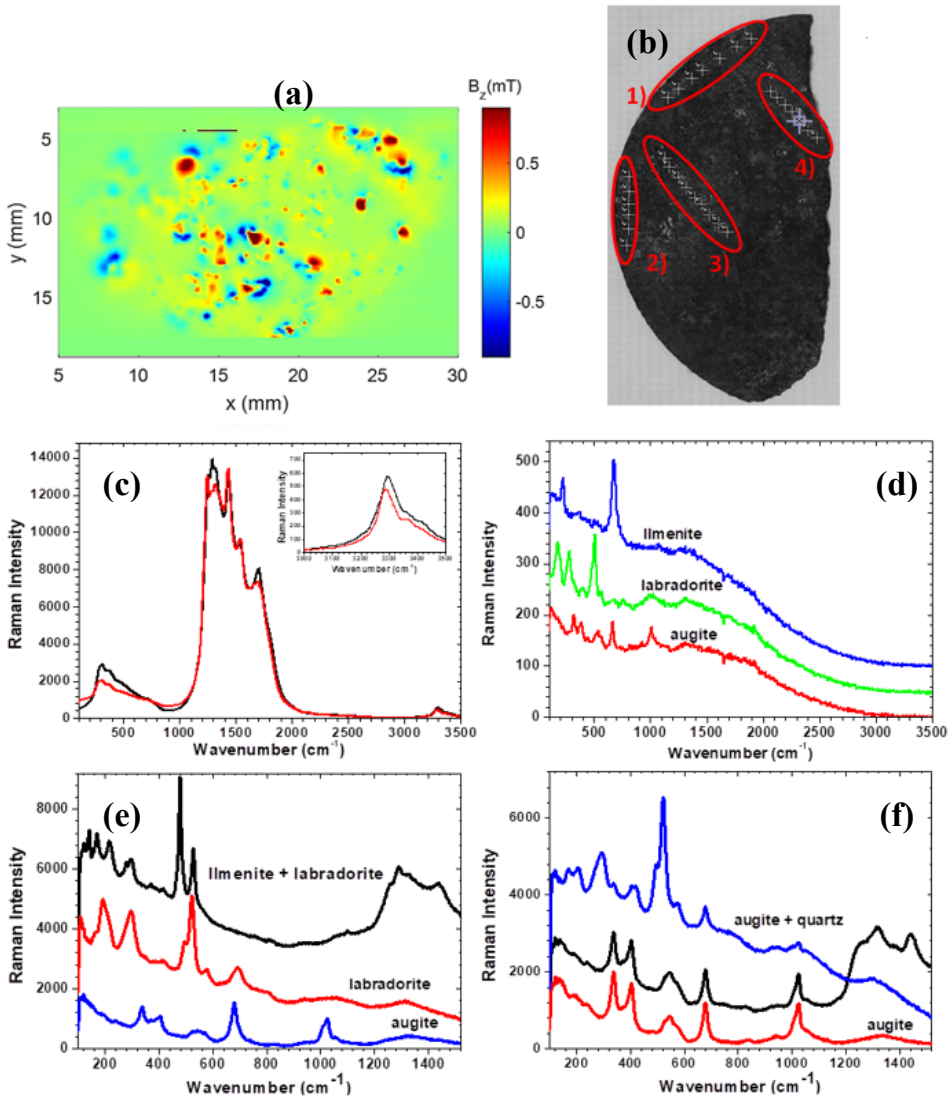

Figure 8. (**a**) Magnetic field image of the Parnaíba sample. (**b**) Optical image with indications of the regions where Raman analysis was performed. (**c-f**) The spectra of regions 1, 2, 3 and 4, respectively.

In the Parnaíba sample, Raman analysis was performed in the 4 different regions shown in Figure 8b. Regions 1 and 2 show a concentration of higher (in red) and lower (in blue) field intensities, respectively. Regions 3 and 4 are the regions indicated in the field map (Figure 8a). When we analyzed the Raman spectra of region 1 (Figure 8c), we observed the presence of three bands in the region of the magnetic field with the greatest intensity. The first band is a band of medium intensity in the spectral region of 200 to 800 cm^{-1}; the second band is a band of high intensity in the region from 1200 to 2000 cm^{-1}; and the last band is a band of low intensity from 3100 to 3500 cm^{-1}. The spectra of region 2 (Figure 8d) have several peaks from 100 to 1100 cm^{-1} in the region of the magnetic field with the lowest intensity; however, these spectra do not show the bands of the regions from 1200 to 2000 cm^{-1} and from 3100 to 3500 cm^{-1}. These spectra were identified using the methods described by Wang [27] and Agarwa [28] for studying geological samples such as ilmenite, labradorite and augite ores (Figure 8d) or a combination of them (Figure 8e and 8f); these ores were responsible for the low intensity fields (the blue regions in the magnetic field map). The spectrum of region 1 (Figure 8c) is characteristic of a sample showing luminescence [29 - 30]. Jasinevicius [31] used Raman spectroscopy to perform vibrational and electronic characterizations of several mineral gems and showed that the presence of chemical elements, such as chromium (Cr^{3+}), samarium (Sm^{3+}) or rare earth elements (Eu^{3+}, Nd^{3+}) caused these gems to luminesce. The spectra of region 1 (Figure 8c) and the spectra of albite and liddicoatite [31] are identical spectra, and both show luminescence

Preprints (www.preprints.org) | NOT PEER-REVIEWED | Posted: 18 October 2019 doi:10.20944/preprints201910.0210.v1

Peer-reviewed version available at Materials 2019, 12, 4154; doi:10.3390/ma12244154

in the regions from 1200 to 2000 cm^{-1} and from 3100 to 3500 cm^{-1}, which leads us to assume that Nd^{3+} is present in ilmenite, labradorite and augite ores and is responsible for the higher intensity fields of the Parnaíba sample (the red regions in the magnetic field map). The presence of luminescent material in the ores is observed and confirmed in the spectra obtained in regions 3 and 4 (Figure 8e and 8f, respectively). The assumption of the presence of Nd^{3+} becomes stronger when comparing the spectra obtained herein with those obtained by Yu for Nd_2O_3 with a 785 nm laser [32]. This spectrum contains the luminescent bands of Nd_2O_3 in the same spectral regions and with identical aspects.

Based on the spectra obtained for the Vredefort sample (Figure 9), we observed bands in the regions from 1200 to 2000 cm^{-1} and from 3100 to 3500 cm^{-1}, similar to the results for the Parnaíba sample but with a lower intensity. The peaks observed in each spectrum in the region from 100 to 1100 cm^{-1} indicate the following ores: ilmenite, albinite and quartz [28, 33 - 34].

Thus, it can be stated that the ores that make up each sample are ilmenite, labradorite, and augite for the Parnaíba sample and ilmenite, albinite, and quartz for the Vredefort sample. In addition, Nd^{3+} is assumed to be the luminescent material for both samples.

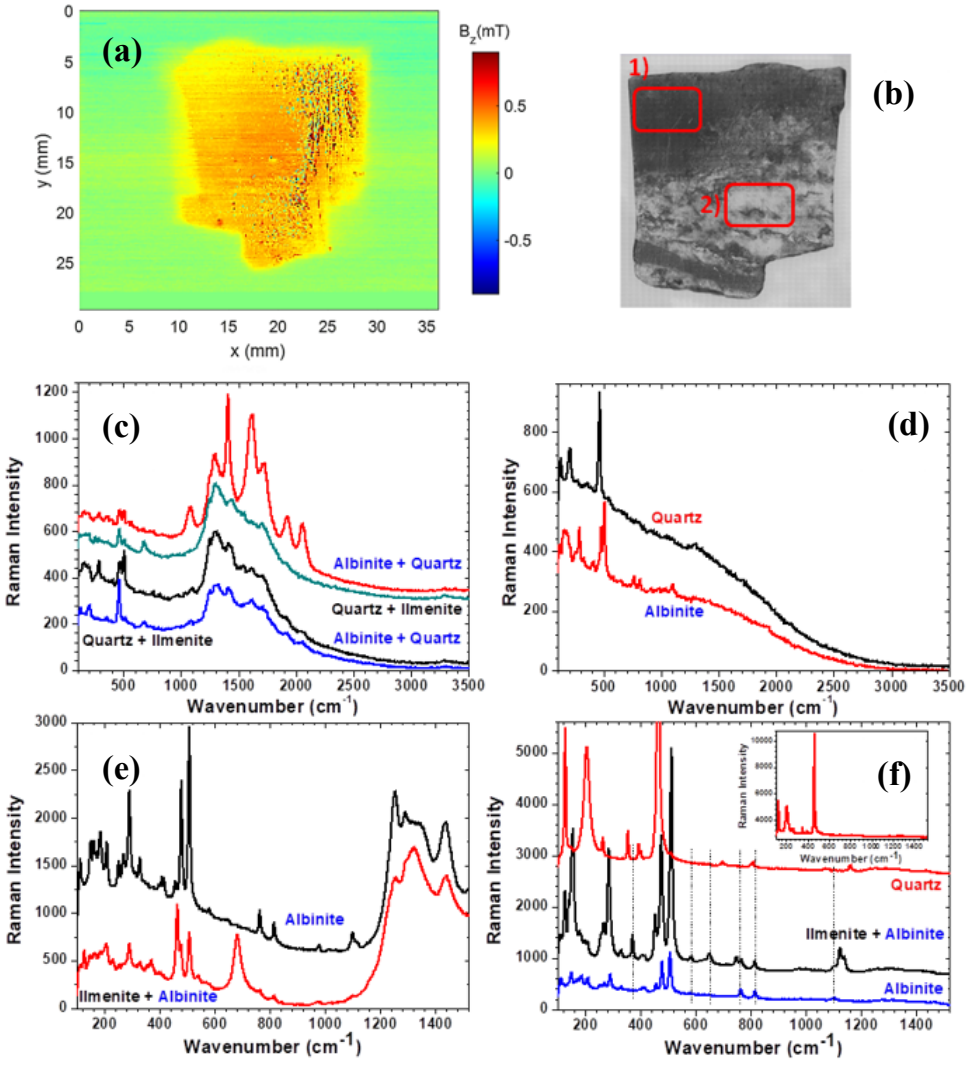

Figure 9. (**a**) Magnetic field image of the Vredefort sample. (**b**) Optical image showing the regions where the Raman analyses were carried out. (**c** and **f**) The respective spectra of regions 1 and 2.

4. Conclusion

We developed a scanning magnetic microscope with a reading system composed of only circuit boards that we built with low operating costs. To demonstrate the capacity of the instrument, thin

and polished sections of the geological samples were successfully scanned along with a sample containing magnetic micro and nanoparticles. After analyzing the magnetic field images of the geological samples, a variation in the magnetic field intensity was observed. Additionally, magnetic field sensitivities better than 521 $nT_{rms}/\sqrt{Hz}$ were obtained between 0.1 and 10 Hz, corresponding to a magnetic momentum sensitivity of 9.20×10^{-10} Am^2. Through Raman spectroscopy analysis, it was demonstrated that the different intensities are related to the presence of different minerals in these samples. These results showed that the reading system is equivalent to commercial lock-in equipment and is a good approximation with respect to the analysis of noise. The significant advantages of this tool over other instruments is that its operation does not require cryogenic technology, reducing its operational cost and complexity. In addition, we showed an application of the equivalent-layer technique to invert the vertical component of the magnetic field generated by the Vredefort sample. In contrast to the Fourier domain approach, we calculated the three components and the amplitude of the magnetic field formulating an inverse problem in the spatial domain.

Acknowledgments: This work was supported in part by the Brazilian agencies CNPq, Capes, Faperj and Fapesp. We thank Fredy Osorio for Figure 1. (b). A special acknowledgment goes to and Dr. Wagner Wlysses for reviewing the manuscript.

References

1. Oda, H.; Kawai, J.; Miyamoto, M.; Miyagi, I.; Sato, M.; Noguchi, A.; Yamamoto, Y.; Fujihira, J.; Natsuhara, N.; Aramaki, Y.; Masuda, T.; Xuan C. E. Plan. Space. 2016, 68, 1-19. doi: 10.1186/s40623-016-0549-3
2. Wit, M.; Welker, G.; Flux compensation for SQUID-detected Magnetic Resonance ForceMicroscopy., J. Magn. Magn. Mater. 2019, 98, 67-70. doi: 10.1016/j.cryogenics.2019.01.001
3. Lazarides, N.; Hizanidis, J.; Tsironis, G. ,P.; ControlledgenerationofchimerastatesinSQUIDmetasurfacesusingDCfluxgradients. 2020, 130, 109413. doi: 10.1016/j.chaos.2019.109413
4. Hamasaki, A.; Furuse, A.; Sekinuma, Y.; Fujio, K.; Iide, M. and Ozeki, S. Improving the Micropore Capacity of Activated Carbon by Preparation under a High Magnetic Field of 10 T. Scient. Report., 2019, 9, 7489. doi: 10.1038/s41598-019-43818-y
5. Hui, F. and Lanza, M. Scanning probe microscopy for advanced nanoelectronics. Nat. Eletroc., 2019, 2, 221-229. doi: 10.1038/s41928-019-0264-8
6. Teixeira, J.M.; Lusche, R.; Ventura, J.; Fermento, R.; Carpinteiro, F.; Araujo, J.P.; Sousa, J.B.; Cardoso, S.; Freitas, P.P.; Rev. Sci. Instrum. 2011, 82, 043902–43906, doi: 10.1063/1.3579497.
7. Araujo, J. F.D.F.; Costa, M. C.; Louro, S. R.W.; Bruno, A.C.; A portable Hall magnetometer probe for characterization of magnetic iron oxide nanoparticles. J. Magn. Magn. Mater. 2017, 426, 159–162. doi: 10.1016/j.jmmm.2016.11.083
8. Araujo, J.F.D.F.; Bruno, A.C.; Carvalho, H.R. Characterization of magnetic nanoparticles by a modular Hall magnetometer. J. Magn. Magn. Mater. 2010, 322, 2806–2809. doi: 10.1016/j.jmmm.2010.04.034
9. Araujo, J. F. D. F.; Pereira, J. M., B.; Bruno, A., C. Assembling a magnetometer for measuring the magnetic propertiesof iron oxide microparticles in the classroom laboratory. Am. J. Phy. 2019, 87, 471-475. doi: 10.1119/1.5100944
10. Araujo, J. F.D.F; Pereira, J.M.B.; Bruno, A. C. Assembling a magnetometer for measuring the magnetic properties of iron oxide microparticles in the classroom laboratory. Am. J. Phys., 2019, 87, 471-475. doi: 10.1119/1.5100944
11. Araujo, J. F. D. F.; Bruno, A.C.; Louro, S. R. W. Versatile magnetometer assembly for characterizing magnetic properties of nanoparticles. Rev. Sci. Instrum. 2015, 85, 105103-7. doi: 10.1063/1.4931989
12. Araujo, J. F. D. F.; Vieira, D. R. P.; Osorio, F.; Pöttker, W. E.; Porta, F. A.; Presa, P.; Perez, G.; Bruno, A. C. Versatile Hall magnetometer with variable sensitivity assembly for characterization of the magnetic properties of nanoparticles. J. Magn. Magn. Mater. 2019, 489, 165431–165431. doi: 10.1016/j.jmmm.2019.165431

13. Klein, T.; Shpringer, I.; Fikler, B.; Elbaz, G.; Cohen, S.; Yakir, D.; Relationships between stomatal regulation, water-use, and water-use efficiency of two coexisting key Mediterranean tree species. For. Eco. Managem. 2013, 302, 34–42. doi: 10.1016/j.foreco.2013.03.044
14. Pilkington, M.; Grieve, R. A. F.; The geophysical signature of terrestrial impact craters. A.G.U. 1992, 30, 2. doi: 10.1029/92RG00192
15. Pilkington, M.; Hildebrand, A. R.; Transient and disruption cavity dimensions of complex terrestrial impact structures derived from magnetic data. A.G.U. 2003, 30, 21. doi: 10.1029/2003GL018294
16. Yokoyama, E.;Nédélec, A.;Baratoux, D.;Trindade, R. I. F.;Fabre, S.; Berger, G.; Hydrothermal alteration in basalts from Vargeão impact structure, south Brazil, and implications for recognition of impact-induced hydrothermalism on Mars. Icarus. 2015, 252, 347-365. doi: 10.1016/j.icarus.2015.02.001
17. Carporzen, L.; Gilder, S. A.; Hart, R. J.; Palaeomagnetism of the Vredefort meteorite crater and implications for craters on Mars. Nature. 2005, 435, 198-201. doi: 10.1038/nature03599
18. Berghofer, L. K.; Hocking, A. D.; Miskelly, D.; Jansson, E.; Microbiology of wheat and flour milling in Australia. Int. J. Fo. Microb. 2003, 85, 137–149. doi: 10.1016/S0168-1605(02)00507-X
19. Salminen, A.; Kaarniranta, K.; Kauppinen, A.; Ojala, J.; Haapasalo, A.; Soininen, H.; Hiltunen, M.; Impaired autophagy and APP processing in Alzheimer's disease: The potential role of Beclin 1 interactome. Prog. Neur. 2013, 106-107, 33-54. doi: 10.1016/j.pneurobio.2013.06.002
20. Passchier, C. W.; Pseudotachylyte and the development of ultramylonite bands in the Saint-Barthélemy Massif, French Pyrenees. J. Struc. Geo. 1982, 4, 69-79. doi: 10.1016/0191-8141(82)90008-6
21. Dressler, B. O.; Reimold, W. U.; Order or chaos? Origin and mode of emplacement of breccias in floors of large impact structures. Earth-Science Rev. 2004, 67, 1-54. doi: 10.1016/j.earscirev.2004.01.007
22. E. A. Lima and B. P. Weiss. Obtaining vector magnetic field maps from single-component measurements of geological samples. Journal of Geophysical Research: Solid Earth, 114(B6), 2009.
23. J. S. Lourenco and H. F. Morrison. Vector magnetic anomalies derived from measu-rements of a single component of the field. GEOPHYSICS, 38(2):359–368, 1973.
24. S.-L. Li and Y. Li. Inversion of magnetic anomaly on rugged observation surface in the presence of strong remanent magnetization. GEOPHYSICS, 79(2):J11–J19, 2014.
25. C. Lana, R. L. Gibson, W. U. Reimold, and R. C. Minnitt. Geology and geochemistry of a granite-greenstone association in the southeastern Vredefort dome, South Africa. South African Journal of Geology, 106(4):291–314, 12 2003.
26. L. Uieda, V. C. O. Jr, and V. C. F. Barbosa. Modeling the earth with fatiando a terra. In S. van der Walt, J. Millman, and K. Huff, editors, Proceedings of the 12th Python in Science Conference, pages 96 – 103, 2013.
27. Alian Wang, Karla E. Kuebler, Bradley I. Jolliff, and Larry A. Haskin. Raman spectroscopy of Fe-Ti-Cr-oxides, case study: Martian meteorite EETA79001. American Mineralogist 2004, 89, 665–680. doi: 10.2138/am-2004-5-601.
28. Amar Agarwal, Boris Reznik, Agnes Kontny, Stefan Heissler, Frank Schilling. Lingunite-a high-pressure plagioclase polymorph at mineral interfaces in doleritic rock of the Lockne impact structure (Sweden). Scientific Reports, 2016, 6, 1-9. doi: 10.1038/srep25991.
29. M. Gaft, R. Reisfeld, G. Panczer, Ph. Blank, G. Boulon. Laser-induced time-resolved luminescence of minerals. Spectrochimica Acta Part A: Molecular and Biomolecular Spectroscopy. 1998, 54, 2163–2175. doi: 10.1016/S1386-1425(98)00134-6.
30. Christoph Lenz, Lutz Nasdala, Dominik Talla, Christoph Hauzenberger, Roland Seitz, Uwe Kolitsch. Laser-induced REE3+ photoluminescence of selected accessory minerals — An “advantageous artefact” in Raman spectroscopy. Chemical Geology, 2015, V 415, pp 1–16. doi: 10.1016/j.chemgeo.2015.09.001.
31. Renata Jasinevicius, Bob Downs. Characterization of Vibrational and Electronic Features in the Raman Spectra of Gem Minerals. Master of Science, University of Arizona. 2009.
32. Jinqiu Yu, Lei Cui, Huaqiang He, Yunsheng Hu, Hao Wu, Jia Zeng, Yuzhu Liu. Laser-excited luminescence of trace Nd3+ impurity in LaBr3 revealed by Raman spectroscopy. Chemical Physics Letters 2012, V 549, pp 32–38. doi: 10.1016/j.cplett.2012.08.039.
33. Wei Tan and Peng Liu. Mineralogy and Origin of Exsolution in Ti-rich Magnetite from different Magmatic Fe-Ti oxide-bearing intrusions. The Canadian Mineralogist. 2016, vol. 54, pp. 539-553. doi: 10.3749/canmin.1400069.

34. Ágnes Görög, Eszter Balassi & Tamás Váczi. Nothia ex gr. excelsa (Grzybowski, 1898), 'flysch-type' agglutinated foraminifera from the Karpatian (Early-Miocene) of Hungary. Historical Biology, 2017. .doi: 10.1080/08912963.2016.1278444.